Online Predictive Modeling of the Thermal Effect of Bio-Implants with Spatially Distributed Parameters

Ayca Ermis, *Student Member, IEEE,* Yen-Pang Lai, and Ying Zhang, *Senior Member, IEEE*

Abstract— **With the increased functionality of implantable medical devices (IMDs), real-time thermal management of these devices has gained growing attention to prevent overheating in the surrounding tissue of IMDs in certain applications, such as neural prostheses like deep brain stimulators (DBS). In this paper, a novel identification method is developed to predict the thermal dynamics of bio-implants, e.g. Utah electrode array (UEA). The proposed method adopts a thermal model with multiple heat sources to characterize the thermal dynamics of IMDs with multiple modules using the data collected by spatially distributed heat sensors. Algorithm predicts the temperature readings of heat sensors in an online fashion within a time window and updates the system parameters iteratively to improve the performance of the algorithm. Algorithm validation is realized using COMSOL software simulations as well as using an in vitro experimental system.**

Index Terms— **implantable medical devices, predictive modeling, spatial estimation, subspace identification, thermal effect**

I. INTRODUCTION

WITH the increased functionality of implantable medical devices (IMDs) in monitoring, recording neural signals and providing required stimulation for medical purposes, IMDs have gained prominence in the modern society. Such improved capabilities may lead to damage in the surrounding tissue of IMDs due to overheating of electrodes in certain applications, such as neural prostheses like deep brain stimulators (DBS) [1] and electrodes for intraoperative electrostimulation used in brain glioma surgeries [2]. Many neural prostheses interact with the central or the peripheral nervous system and help to restore motor, sensory or cognitive functionality that may have been damaged while continuously communicating with external devices for monitoring and recording purposes. For the neural IMDs, low power consumption is of importance to maintain the long-term operation of the device and to protect patient's health and safety. Due to their continuous operation and its close proximity to living tissues, any overheating caused by the IMD may lead to permanent damage to these soft tissues [3]. For example in DBS, strong energy fields and administration of electrical currents, such as electrocautery, can lead to overheating of the electrodes with a risk of damage in the surrounding brain tissue [1]. Another origin of potential damage to the tissue is the electrical stimulation-induced tissue injury (overstimulation) [4]. European standards for active IMDs require that the maximum temperature of the outer surface of the implant does not exceed the normal body

temperature by $2°C$ [5]. In [6], authors discuss an incident in which a patient with an implanted DBS suffered a serious brain damage due to overheating in brain tissue surrounding the DBS in response to diathermy and the patient subsequently died.

The thermal effect of implantable devices has been studied in previous literature. In [7], the author studies various causes of temperature increase of a dual-unit retinal prosthesis and how to model its thermal effect. According to [7], the causes of the overheating in the surrounding tissue of the IMD include telemetry coil, electrodes used for stimulation and electromagnetic field induced in the body in addition to the power dissipation of the implanted microchip. The Pennes bioheat transfer equation is proposed to model this thermal effect of the IMDs [7]. Finite element analysis (FEA) is used to solve the Pennes bioheat equation in [8] and similarly in [9], FEA and finite difference time domain (FDTD) are proposed to solve the Pennes bioheat equation. FEA and FDTD methods solve for the heat dissipation and electromagnetic field for the whole computational domain for each time instance. Due to their space and time complexity, these aforementioned numerical methods are not suitable for real-time applications.

For the real-time thermal management, online prediction of the thermal effect caused by an implantable device has become essential. In [10], Chai *et al.* proposed a recursive multi-step prediction error minimization method (RMSPEM) for online update of the model parameters of a simplified thermal model with a single heat source online to support real-time control. In [11], a predictor-based subspace identification (PBSID) method is proposed, which uses the high-order vector auto-regressive with exogenous inputs (VARX) predictor from [12], since the performance of the VARX predictor compares favorably to other subspace identification algorithms [13]. However, the PBSID method is a centralized system identi-

fication technique and its performance is contingent upon the spatial independence of the data. In [14], the authors implement a recursive PBSID method with batch pre-processing using a VARX model to characterize the thermal effect of bio-implants. In their work, however, the authors neglect the spatial autocorrelation of the data and treat each sensor as a subsystem of the overall system to investigate the performance of PBSID algorithm on characterizing the thermal effect of the system with multiple power inputs.

With the increase in functionality of IMDs, such as added wireless capabilities etc., many implantable devices contain multiple electronic modules. Considering that each module could contribute to the temperature increase, it has become necessary to include the spatial distribution of the heat dissipation in our model. There have been studies analyzing spatial data, many of which focus mainly on identification of spatially distributed systems, e.g. wireless sensor networks [15] or on ecological modeling [16]. In geo-spatial analysis, different algorithms are utilized, such as geographically weighted regression (GWR), spatial autoregressive modeling (SAR) as well as spatial filtering models [16]. Spatial correlation and time-space separation of data are used previously in [17] to investigate the thermal effect of batteries. In [18], authors introduce a data-driven approach to localize abnormality for distributed parameter systems using dynamic spatial independent component analysis. In [19] and [20], Haber *et al.* introduce a new identification algorithm for spatially varying distributed systems defined on an arbitrary graph. In their work, system matrices of the global system is derived by applying the identification methods introduced in [11] to all local subsystems in the interconnection; thus numerically solving for the spatial correlation of the local subsystems. However, computational complexity of their algorithm is $O(N^2)$. To the authors' knowledge, there have been few studies addressing the online thermal prediction problem of the implantable medical device with multiple spatially distributed subsystems.

In this paper, modeling the thermal dynamics of the IMDs with multiple heat sources is explored and a novel algorithm is proposed to update the model parameters in an online fashion. Goal of developing this online prediction algorithm for the thermal effect of the IMDs is to implement a model-predictive control (MPC) scheme to adjust the power inputs of the electrodes accordingly to prevent permanent damage while maintaining the required performance of IMDs. Herein, we propose an online thermal prediction algorithm which maintains the spatial distribution of heat dissipation and its effect on the temperature increase. Different from the previous work which investigates power dissipation in the circuitry as the only heat source [10], IMDs with multiple modules are investigated whose power consumption can be controlled through the control input, and multiple temperature sensors spatially distributed on the motherboard. Examples of different modules on IMDs may include motherboard, radio module for wireless communication, energy storage device, and so on. To represent such modules of the IMD, multiple heat sources are used. Different from previous works in the literature, our prediction algorithm implements a spatial filter with a novel spatial weights matrix to separate the temperature readings

of heat sensors into two components based on their spatial dependence, thus investigating the effect of heat dissipation in a spatial context. Prediction of the centralized non-spatial, i.e. spatially independent, data component is achieved by utilizing predictor-based identification methods with the predictor model proposed in [11]. This predictor-based identification algorithm is implemented with a first order VARX predictor to model slowly time-varying parameters of a multiple-input system. The spatially dependent component of the temperature data can then be determined by solving the least squares problem of a purely lagged spatial autoregressive (SAR) model. With this online prediction algorithm, thermal effect of the device could be estimated for power inputs and optimal power inputs to prevent overheating could then be selected via MPC.

The remainder of the paper is organized as follows. Following the introduction, Section II presents the system model of implantable device with neural prosthesis as an example. The prediction algorithm with spatial filtering is proposed in Section III. Section IV presents the simulation studies and in vitro experiments of the proposed method. In section V, performance and computational cost of the proposed algorithm is compared with alternative algorithms introduced in [11], [19] and [20]. At last, conclusions are derived in Section VI.

II. SYSTEM DESCRIPTION

As described in [21], system components of neural prosthesis include optics module, power module, radio module and motherboard module. For our investigation, 3-D Utah electrode array (UEA) is selected as the microelectrode array, since it has become a benchmark for neural recording and its thermal effect has been studied in previous works [8], [9]. The system diagram introduced in [10], which is created based on system components presented in [21], is adopted in this paper, since it is relatively comprehensive. The motherboard module consists of the microcontroller and power circuitry. The radio module provides wireless communication between a laptop or computer and the system for data transmission. Control signals for power consumption of the system is also transmitted via the radio module. In this paper, an energy storage device, e.g. battery or supercapacitor, is not implemented on the testing vehicle, but its contribution to the temperature increase is investigated by modeling it as a heat source. A diagram of the system adopted in this paper is presented in Figure 1.
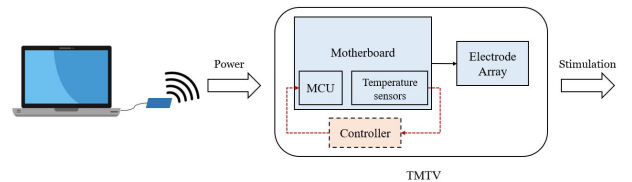

Fig. 1: Diagram showing the multiple components of the system.

In our work, temperature increase induced by the aforementioned modules of the neural IMD is modeled as multiple heat sources. The temperature change is measured via multiple

on-board temperature sensors. The system dynamics to be modelled can be formulated with a one-step ahead predictor as follows

$$\hat{y}_{k|k-1} = \sum_{i=0}^{p} \alpha_i u_{k-i} + \sum_{j=1}^{p} \beta_j y_{k-j}^{f} + f(W_{k-1} y_{k-1}^{sp}) + \varepsilon \tag{1}$$

where y^f is the filtered non-spatial component of the temperature data obtained by the sensors, y^{sp} is the spatial component of the temperature data obtained by the sensors, $u_k \in \mathbb{R}^r$ is the input vector, $\hat{y}_{k|k-1} \in \mathbb{R}^l$, W is the spatial weights matrix at time instance k and α, β are the set of parameters to be estimated. The method for constructing the spatial weights matrix is described in Section III.A.

Since temperature recording of each temperature sensor depends on its location with respect to all heat sources, spatial dependence of temperature readings cannot be neglected. Thus, it is necessary to introduce a spatial filtering method to separate the temperature data into two components based on its spatial dependency, i.e. filtered spatial component vs. non-spatial component. This spatial filtering method is further explained in Section III.

III. ONLINE PREDICTION ALGORITHM

The first step of the proposed algorithm is to apply a spatial filter to the sensor data to separate its spatially dependent from independent components. After spatial filtering, a SAR model is used with a kernel recursive least squares (KRLS) adaptive filter to model the spatial distribution of the data, while PBSID methods are utilized to predict the centralized spatially independent component of the temperature data. Main steps of the overall algorithm is shown in Figure 2. After the prediction step at each time instant k, prediction results for both spatial and non-spatial components are combined to obtain an overall prediction of the system.
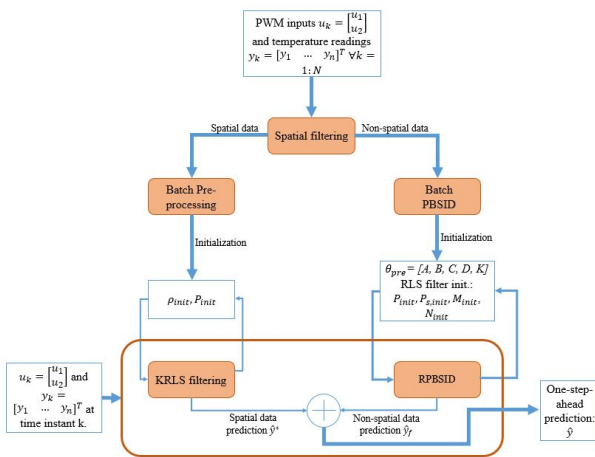

Fig. 2: Diagram of the overall prediction algorithm.

A. Spatial Filtering

Spatial filtering methods are used to partition spatially autocorrelated data into two components, one of which contains the spatially dependent data and the other component

is the spatially independent data. In [22], Getis and Griffith apply spatial filtering to potentially independent variables in a regression equation using two different methods. The first method in [22], i.e. Getis method, uses Getis-Ord statistic G_i to convert spatially correlated data into two variates, one of which captures the spatial correlation and the other variate contains the filtered non-spatial variable [23]. In the second method, i.e. Griffith method, the spatially independent variable could be obtained by removing its embedded spatial pattern similar to the Getis method using linear combinations of connectivity matrix eigenvectors [24]. However, the Griffith method assumes the spatial pattern of the system is known and thus, a binary geographic connectivity matrix C is available. In our work, the connectivity matrix of temperature sensors is not explicitly available. Thus, the Getis method is chosen for spatial filtering to examine the local spatial association among temperature sensors.

The main assumption of our work is that all sensors contribute to spatial dependence of temperature readings due to close proximity of the sensors. Thus, the appropriate distance d, within which nearby sensors are spatially dependent, is selected as the radius of the circle encompassing the implantable device. Then for each sensor $i = 1, 2, ..., n$, spatial contributions of all other sensors on the selected sensor i is computed with the local Getis-Ord G_i statistic as

$$G_i(d) = \frac{\sum_j w_{ij} \cdot y_j}{\sum_j y_j}, i \neq j \tag{2}$$

where i is the observation point, i.e. the selected sensor, y_j denotes the observed temperature readings at the neighboring sensor j and w_{ij} corresponds to the element at the i-th row and j-th column of $n \times n$ weights matrix W. Different from the conventional choice of the weights matrix W, which is a binary matrix indicating the neighbors, the weights matrix W is constructed to be inversely proportional to the distance between sensors s_i and s_j, i.e. $w_{ij} = \frac{1}{|s_i - s_j|}$ for $i \neq j$ and $W[i,i] = 0$ to describe the correlation between each sensor locations. The matrix W is then normalized via maximum eigenvalue normalization. In addition to the correlation between the sensor locations, another measure describing the spatial thermal effect of the heat sources at sensor locations is added to the weights matrix W. The heat dissipation from each heat source is can be modeled as a multi-variate Gaussian distribution. Since the heat generated at each heat source is dependent on its power input, this additional measure at sensor s_i can be computed as $m_i = u_1 p_1(s_i) + \cdots + u_r p_r(s_i)$ where u denotes the power input for the corresponding heat source, r is the number of heat sources and p denotes the density function of the corresponding Gaussian distribution. Thus, the spatial filtering becomes dependent on the inputs at the given time instance. The measure m_i is normalized with respect to the maximum eigenvalue λ_{max} of the weights matrix and added to the diagonal of W.

$$W = \begin{bmatrix} m_1 & w_{12} & \cdots & w_{1n} \\ w_{21} & m_2 & \cdots & w_{2n} \\ \vdots & & \ddots & \vdots \\ w_{n1} & \cdots & w_{n(n-1)} & m_n \end{bmatrix} \cdot \frac{1}{\lambda_{max}} \tag{3}$$

The calculated G_i statistics at given sensor locations are then compared to the expected value of contribution in spatial dependence embedded in the original variable, which is of the form $E_i(d) = \frac{\sum_j w_{ij}}{(n-1)}$ where n is the number of observations [22]. The source data y can then be transformed into its filtered non-spatial component, which is averaged across all sensor locations to minimize measurement errors with the following equation

$$y^f = \frac{1}{n} \sum_i y_i \frac{E_i(d)}{G_i(d)} = \frac{1}{n(n-1)} \sum_i \sum_j \frac{w_{ij}y_i}{G_i(d)} \quad (4)$$

Since the original temperature data is a sum of both components, i.e. $y = y^{sp} + y^f$, the spatial component is can then be calculated as $y^{sp} = y - y^f$.

B. Identification of Non-spatial Data Component

For online prediction of the non-spatial component, i.e. y^f, we utilize identification methods proposed in [11], [25]. A vector autoregressive model with exogenous inputs (VARX) is chosen to model the thermal dynamics of the multiple-input, single-output (MISO) system. One-step-ahead VARX predictor can be written as

$$\hat{y}^f_{k|k-1} = \sum_{i=0}^p \alpha_i u_{k-i} + \sum_{i=1}^p \beta_i y^f_{k-i} \quad (5)$$

where $\hat{y}^f_{k|k-1}$ is the predicted output of the subsystem at time instant k using a finite window of past inputs and outputs. p denotes the length of the finite window of past data. $\bar{\Xi} := \begin{bmatrix} \alpha_p & \alpha_{p-1} & ... & \alpha_0 & \beta_p & ... & \beta_1 \end{bmatrix} \in \mathbb{R}^{l \times p(r+l)+r}$ is the set of VARX paramaters to be estimated. Using the VARX model, we can estimate Markov parameters of the system as shown in [11], [25].

1) Regularized Batch Pre-processing: Prior to online prediction, a batch of data is used to determine initial values for Markov parameters of the centralized non-spatial system. This procedure is called batch pre-processing. The first step in batch pre-processing is to construct stacked matrices U, Y^f, and Hankel matrices for $\bar{Y}^f_p$ and $\bar{U}_p$ as shown in [11]. Using these stacked matrices, parameters of the linear VARX predictor in (5) can be estimated using least squares regression as follows:

$$\begin{aligned} \bar{\Xi} &= Y^f \Psi^T (\Psi \Psi^T + \mu I)^{-1} \\ \Psi &= \begin{bmatrix} \bar{U}_p^T & U^T & \bar{Y}_p^{fT} \end{bmatrix}^T \end{aligned} \quad (6)$$

where μ is the Tikhonov regularization term selected to minimize the estimation error via 10-fold cross-validation.

After computing the VARX predictor parameters $\bar{\Xi}$, product of the extended observability matrix and state sequence, $\widehat{\Gamma X}$, can be computed as $\widehat{\Gamma X} = \begin{bmatrix} \hat{\alpha}_p & \hat{\alpha}_{p-1} & ... & \hat{\alpha}_1 \end{bmatrix} \bar{U}_p + \begin{bmatrix} \hat{\beta}_p & \hat{\beta}_{p-1} & ... & \hat{\beta}_1 \end{bmatrix} \bar{Y}^f_p$. We derive the predicted full state sequence $\hat{X}$ from $\widehat{\Gamma X}$ sequence by solving the rank-n approximation of the SVD. System matrices A, B, C, D, and the Kalman gain K can be computed by solving the second linear problem in (1) with the batch least squares method.

2) Recursive Predictor-based Subspace Identification: Recursive predictor-based subspace identification method updates the model parameters iteratively. For this method, the system parameters obtained from batch pre-processing is used for initialization.

Adaptive filters, more specifically recursive least squares (RLS) filters, are implemented to track time-varying dynamics of the system, and a forgetting factor is added to ensure the past data becomes less relevant for the current estimation.

For recursive prediction, VARX predictor in (5) is re-written in the linear regression form

$$y^f_k = \tilde{\Xi}_k \psi_k + e_k \quad (7)$$

where $\psi_k = \begin{bmatrix} u_p^T & u_k^T & y_p^{fT} \end{bmatrix}^T$, u_p and y_p are the vectors of past p data points at time instant k. Different from batch pre-processing, $\tilde{\Xi}$ is defined as an adaptive filter of the form

$$\tilde{\Xi}_k = \tilde{\Xi}_{k-1} + (y^f_k - \tilde{\Xi}_{k-1}\psi_k)\psi_k^T P_k \quad (8)$$

Error covariance matrix P_k is initialized at $P_i = (\frac{1}{\rho_1})I$ with $\rho_1 > 0$ and P_k is updated iteratively with

$$P_k = \frac{1}{\lambda_1} P_{k-1} - \frac{1}{\lambda_1} P_{k-1}\psi_k(\lambda_1 I + \psi_k^T P_{k-1}\psi_k)^{-1}\psi_k^T P_{k-1} \quad (9)$$

where $1 \geqslant \lambda_1 \gg 0$ is the forgetting factor. Common values for the forgetting factor λ are between $0.995 > \lambda > 0.95$; thus, $\lambda = 0.99$ is selected for the RLS filter in the algorithm to minimize the prediction error via 10-fold cross-validation.

The state vector $\hat{x}_k$ can then be estimated from the past input-output data, i.e. u_p and y_p as $\hat{x}_k = S(\begin{bmatrix} \hat{\alpha}_p & \hat{\alpha}_{p-1} & ... & \hat{\alpha}_1 \end{bmatrix} u_p + \begin{bmatrix} \hat{\beta}_p & \hat{\beta}_{p-1} & ... & \hat{\beta}_1 \end{bmatrix} y^f_p)$ at time instant k, where selection matrix S is determined via projection approximation subspace tracking (PAST) method proposed in [26] and has an adaptive filter update. Once the state vector $\hat{x}_k$ is estimated, system matrices A_k, B_k, C_k, D_k, and the Kalman gain K_k are computed by updating the corresponding RLS filters.

C. Identification of Spatial Data Component

With the available spatial data components of the temperature data, one-step-ahead spatial component of each sensor can be estimated by solving the least squares problem of a nonlinear pure spatially lagged autoregressive (SAR) model. The nonlinear SAR model at sensor location i can be written as

$$y^{sp}_i = f_i(W_i y^{sp}_i) + \mathcal{E}_i \quad (10)$$

For recursive prediction, one-step ahead predictor using the nonlinear SAR model can be written in the regression form as

$$y^{sp}_{k|k-1} = f(\phi_{k-1}) + \mathcal{E}_k \quad (11)$$

where $\phi_{k-1=W_{k-1}y^{sp}_{k-1}}$ with $n \times 1$ stacked vector of spatial data components of each sensor location y^{sp}_{k-1} and $\mathcal{E}_k$ is the $n \times 1$ error vector which contains the prediction error. A KRLS filter is then implemented to estimate the nonlinear function $f_i(.)$ that relates the input ψ_k to the output $y_k = f_i(\psi_k)$ according to this SAR model. As part of the KRLS filter,

the following Gaussian kernel with $\sigma = 0.95$ is selected; $\kappa(\psi_i, \psi_j) = exp(-\frac{\|\psi_i - \psi_j\|^2}{2\sigma^2})$. Using the KRLS filter theory, the nonlinear function $\hat{f}(\psi)$ can then be formulated as $f(\psi) = \sum_{i=1}^{m_{k-1}} \rho_i \kappa(\psi_i, \psi)$ where ρ_i is the weight for corresponding kernel result $\kappa(\psi_i, \psi)$ and m_{k-1} denotes the number of data points admitted to the dictionary and used for estimation at each instant. A dictionary $D_{k-1} = \{(\hat{\psi}_i, \hat{y}_i)\}_{i=1}^{m_{k-1}}$ has been constructed from a subset of size m_{k-1} of the received vectors.

For our work, surprise criterion (SC) is chosen as a sparsification technique since it examines the relation between the inputs of the incoming data and those of the dictionary and computes the approximation error to determine when to add a new data point into the dictionary [28]. Surprise is an information measure of the new sample with respect to the vectors in the dictionary and can be defined as $S_k = \frac{1}{2} \ln \delta_k + (y_k^{sp} - \mathbf{k}_{k-1}^T \rho_{k-1})^2 / 2\delta_k$ where δ_k is the approximate linear dependence (ALD) measure. Using the kernel trick, the ALD measure δ_k can be expressed as $\delta_k = k_{kk} - \mathbf{k}_{k-1}^T \mathbf{a}_k$ where $k_{kk} = \kappa(\phi_k, \phi_k)$, $\mathbf{k}_{k-1}$ is a matrix with entries $[\mathbf{k}_{k-1}]_i = \kappa(\hat{\phi}_i, \phi_k)$, and $\mathbf{a}_k = \mathbf{K}_{k-1}^{-1} \mathbf{k}_{k-1}$ with the kernel matrix $[\mathbf{K}_{k-1}]_{i,j} = \kappa(\hat{\phi}_i, \hat{\phi}_j)$. Surprise criterion parameters T_1 and T_2 are determined via a 10-fold crossvalidation on the batch data. The input-output data at time instant k is added to the dictionary only if it is classified as learnable, i.e. the surprise measure S_k lies in the interval $[T_1, T_2]$ [29]. If the SC test is passed and new vectors are added to the dictionary, the following KRLS update equations are applied:

$$\mathbf{K}_k^{-1} = \frac{1}{\delta_k} \begin{bmatrix} \delta_k \mathbf{K}_{k-1}^{-1} + \mathbf{a}_k \mathbf{a}_k^T & -\mathbf{a}_k \\ -\mathbf{a}_k^T & 1 \end{bmatrix}$$

$$\mathbf{P}_k = \begin{bmatrix} \mathbf{P}_{k-1} & 0 \\ 0^T & 1 \end{bmatrix} \quad (12)$$

$$\rho_k = \begin{bmatrix} \rho_{k-1} - \frac{\mathbf{a}_k}{\delta_k}(y_k^{sp} - \mathbf{k}_{k-1}^T \rho_{k-1}) \\ \frac{1}{\delta_k}(y_k - \mathbf{k}_{k-1}^T \rho_{k-1}) \end{bmatrix}$$

Alternatively, if the surprise value does not pass the SC test, the dictionary remains unchanged. Then the covariance matrix $\mathbf{P}_k$ and the weight vector ρ_k are updated via the KRLS recursions [27] as follows:

$$q_k = \frac{\mathbf{P}_{k-1} \mathbf{a}_k}{1 + \mathbf{a}_k^T \mathbf{P}_{k-1} \mathbf{a}_k}$$

$$\mathbf{P}_k = \mathbf{P}_{k-1} - q_k \mathbf{a}_k^T \mathbf{P}_{k-1} \quad (13)$$

$$\rho_k = \rho_{k-1} - \mathbf{K}_k^{-1} q_k (y_k^{sp} - \mathbf{k}_{k-1}^T \rho_{k-1})$$

IV. ALGORITHM VALIDATION

Performance of the proposed thermal modeling techniques and online prediction methods with spatial distribution is evaluated with both simulation studies in COMSOL software and *in vitro* experiments.

A. Simulation Studies

Multiphysics modeling software COMSOL is used to simulate the thermal dynamics of the UEA. The UEA model presented in [8] with multiple heat sources is implemented in the COMSOL software as shown in Figure 3. The COMSOL software uses the following Pennes' bioheat equation to model

the heat transfer from the implantable device with multiple heat sources to its surrounding tissues [10]

$$\rho C \frac{\partial T(x,t)}{\partial t} = \nabla \cdot (k \nabla T(x,T)) + A_0 + B_0(T(x,t) - T_b) + \rho SAR + P_{el} \quad (14)$$

where T denotes the temperature in the tissue at spatial coordinates x for instant t, P_{el} is the power density of the implanted device, and ρ and C are the tissue density and specific heat, respectively [10]. According to [10], $\nabla \cdot (k \nabla T(x,T))$ models the thermal diffusion with the thermal conductivity of tissue k. Since the focus of our paper is to model the thermal effect of multiple heat sources with spatial distribution, the heating effect caused by the electromagnetic field, i.e. ρSAR, the effect of blood perfusion, i.e. $B_0(T(x,t) - T_b)$, and heat generation by metabolism, i.e. A_0, are neglected from (11) and are modeled as disturbances to simplify the thermal model.

As shown in Figure 3, the simulation board includes two heat sources ($H1$ and $H2$) and six probes, ($S1 - S6$), to measure the temperature change and the probes are placed at the given coordinates surrounding two heat sources. COMSOL software utilizes the FEA method to solve the Pennes bioheat equation and produces temperature readings of each heat sensor. These temperature readings are then used as a reference to demonstrate the performance of the proposed online prediction algorithm. Using the aforementioned COMSOL model,
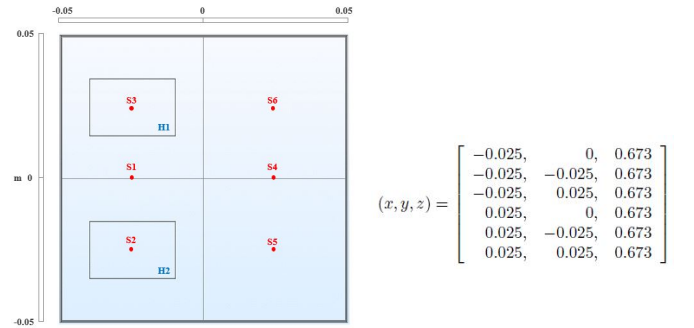

Fig. 3: Board layout in COMSOL software with sensor locations in *red*.

two sets of studies were conducted: (1) 2000 data samples generated using two Gaussian distributions within the range of $[0.279, 0.837]$ Watt (W) are used for the power inputs in the first simulation; and (2) for the second simulation, square wave signals of length 2000 are used to emulate the controller effect on the power input and evaluate the performance of the prediction algorithm when controller is implemented. The upper value, i.e. 0.837, of the Gaussian distributions in study (1) corresponds to the upper limit of operating power inputs. Square wave signals for both inputs in study (2) have the same 50% duty cycle and a period of 20 seconds. For each simulation study, two separate runs are conducted to examine the thermal effect of applying same vs. different power inputs to the two heat sources. The goal of applying inputs with different amplitudes is to investigate the effect of having modules of the IMD operating at different

power levels. In study (2), square wave inputs of amplitude 0.75 W are generated for the case with same inputs. For the case with different amplitudes in study (2), one of the square wave inputs has an amplitude of 0.5 W and the other input has an amplitude of 0.5 W. For all simulation studies, a batch data with randomly generated Gaussian inputs from a previous COMSOL simulation is used for preprocessing. As a result of the 10-fold crossvalidation with the batch data, regularization term λ is set as $\lambda = 86.8$. In addition, thresholds values for surprise criterion T_1 and T_2 are calculated to be $T_1 = 0$ and $T_2 = 20$ via 10-fold crossvalidation.

In Figure 4 and 5, the simulation study results when Gaussian inputs of different amplitudes are applied, are shown. More specifically, in Figure 4, the power inputs are displayed, and Figure 5 shows the comparison between overall prediction results of the algorithm (in red), which consists of prediction results of the spatial data component as well as the non-spatial data component and the temperature readings obtained in COMSOL corresponding to each heat sensor (in blue). For each comparison subplot in Figure 5, a zoomed plot is added to show the comparison of the prediction results and the temperature readings in more detail. As can be seen in Figure 5, the performance of the prediction results improve significantly after approximately 400 seconds. This corresponds to the time it takes for the adaptive filters in the online prediction algorithm to converge. Once the adaptive filters are fully converged, the prediction algorithm can predict the thermal dynamics of the IMD with multiple heat sources with relatively high accuracy. Figure 6 and 7 show the corresponding simulation results for the square wave inputs with different amplitudes. As in Figure 5, a zoomed plot for each comparison plot in Figure 7 is added to show the comparison of the prediction results and the temperature readings in more detail. Similar to the simulation study with Gaussian inputs, the performance of the prediction algorithm in this study improve after the convergence of the adaptive filters at approximately 400 sec.
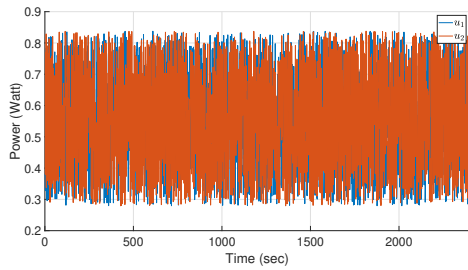

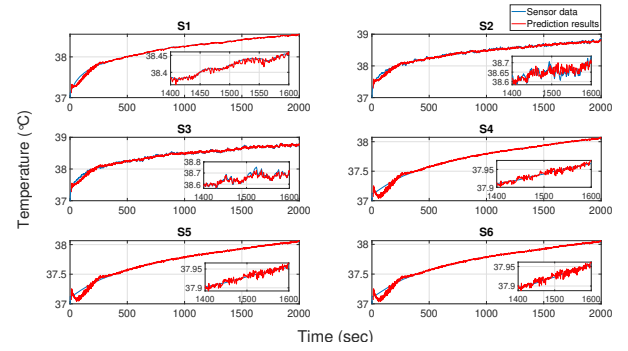Fig. 4: Different randomly generated Gaussian power inputs.

Fig. 5: Simulation results of the spatial and non-spatial data components combined for different Gaussian inputs with local magnification. Each subfigure shows the results for the corresponding sensor probe labeled as S1-S6 in Fig. 3.
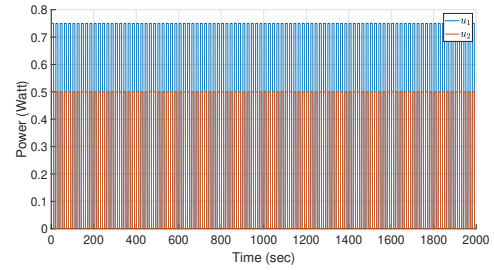

Fig. 6: Square-wave power inputs with different amplitudes which are used to emulate the power inputs to heat sources for evaluating performance of the prediction algorithm when controller is implemented.
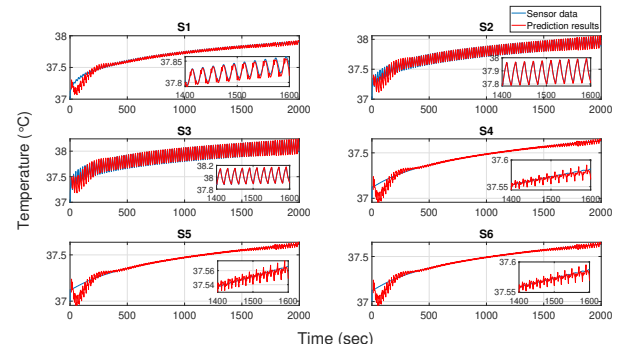

Fig. 7: Simulation results of the spatial and non-spatial data components combined for different square-wave inputs with local magnification. Each subfigure shows the results for the corresponding sensor probe labeled as S1-S6 in Fig. 3.

According to the simulation studies, the size of the dictionary D_k never exceeds 15, i.e. $m \leq 15$. Hence, no pruning is necessary to reduce the size of the dictionary. The comparison between the results of the online prediction algorithm and the temperature readings obtained in COMSOL shows that the proposed algorithm predicts the thermal dynamics of bio-implants with multiple heat sources with relatively high accuracy. The overall MSEs of prediction results at given sensor locations, indicated as S1, S2 etc., are summarized in Table I for each simulation study and Table II summarizes breakdown

of the MSE values of the prediction results obtained via the proposed algorithm into non-spatial identification part vs. spatial identification part of the algorithm. As seen from the MSE values in Table I, the proposed online prediction algorithm predicts the thermal effect with an average mean squared error of 0.938×10^{-3} $^\circ C$ for randomly generated Gaussian inputs and 1.197×10^{-3} $^\circ C$ for square-wave inputs. After convergence of the RLS filters are achieved, i.e. after approximately 400 sec, the averaged MSE values drop to 0.135×10^{-3} $^\circ C$ for randomly generated Gaussian inputs and

TABLE I: MSE RESULTS IN SIMULATION STUDIES ($\times 10^{-3}$ $^{\circ}C$)

S#	Gaussian Inputs		Square-Wave Inputs	
	Same Inputs	Different Inputs	Same Inputs	Different Inputs
S1	1.164	0.755	1.411	1.112
S2	1.137	1.011	1.360	1.182
S3	1.182	1.038	1.319	1.552
S4	0.921	0.729	1.173	0.971
S5	0.927	0.736	1.176	0.963
S6	0.919	0.736	1.171	0.969

TABLE II: NON-SPATIAL & SPATIAL PREDICTION RESULTS IN SIMULATIONS ($\times 10^{-3}$ $^{\circ}C$)

MSE	Gaussian Inputs		Square-Wave Inputs	
	Same Inputs	Different Inputs	Same Inputs	Different Inputs
Non-spatial	1.107	0.873	1.323	1.289
Spatial	0.123	0.124	0.087	0.124

to 0.150×10^{-3} $^{\circ}C$ for square-wave inputs.

B. Experimental Studies

For *in vitro* experiments, a temperature monitoring and management test vehicle (TMTV) with seven temperature sensors (LMT70) and two heat sources (PZT222A) emulating the implanted electronics is used. This test vehicle has been developed based on the previous hardware testing system used in [10] and [14]. The LMT70 temperature sensors on board have a typical accuracy of $\pm 0.05^{\circ}C$ and the thermal power dissipation of each PZT2222A heat source is $1W$ at maximum at an ambient temperature of $25^{\circ}C$. The current version of the testing vehicle has a width of 46.8 mm and a length of 60.15 mm. The layout of the TMTV and the sensor locations are illustrated in Figure 8.

The hardware testing system is shown in Figure 9. For the duration of the experiments, the TMTV is placed in a water-filled container which is shown in the middle of Figure 9. In order to emulate the heat diffusion effect of blood flow, a marine pump and sponge material are placed in the water-filled container. The marine pump is placed at the bottom of the water-filled container to create water circulation. Input voltage of the marine pump is set to $7.5V$ to generate water flow similar to the cerebral blood flow rate of 50 ml/min per $100g$ of tissue [30]. The sponge is placed in the container to ensure a uniform water flow. The water tank is then placed inside an enclosed heat chamber to regulate the environmental temperature. Temperature of the heat chamber is set to $28^{\circ}C$.

A Matlab GUI is created to display and save the temperature measurements and prediction results simultaneously. Continuous temperature data and prediction results for multiple sub-systems can also be displayed simultaneously in the GUI. This Matlab front-end is connected with an nRF52 development kit (nRF52 DK), which acts as the intermediate layer between the TMTV and PC interface. The nRF52 DK communicates with the Bluetooth module (MDBT42Q-512KV2) mounted on the TMTV through Bluetooth protocol and sends pulse-width modulation (PWM) signals to heat sources on the TMTV to generate different amounts of heat. nRF52 DK also sends a control signal to temperature sensors through the Bluetooth module to switch sensors in a sequence. Temperature readings from the sensors are digitalized by an embedded 12-bits
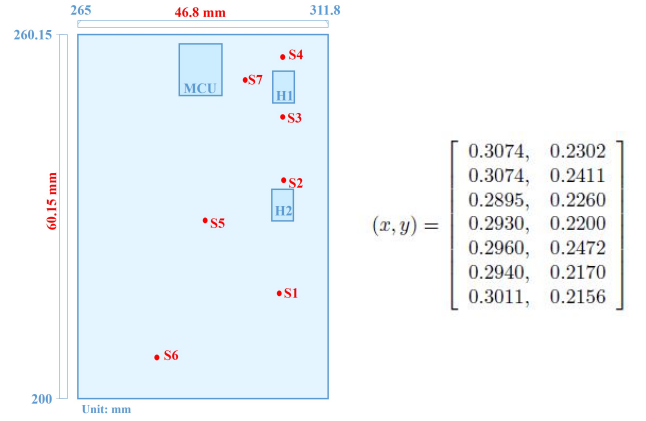

$$(x, y) = \begin{bmatrix} 0.3074, & 0.2302 \\ 0.3074, & 0.2411 \\ 0.2895, & 0.2260 \\ 0.2930, & 0.2200 \\ 0.2960, & 0.2472 \\ 0.2940, & 0.2170 \\ 0.3011, & 0.2156 \end{bmatrix}$$

Fig. 8: TMTV layout with two heat sources (*H1, H2*) and seven temperature sensors shown in *red* and coordinates of the sensors.
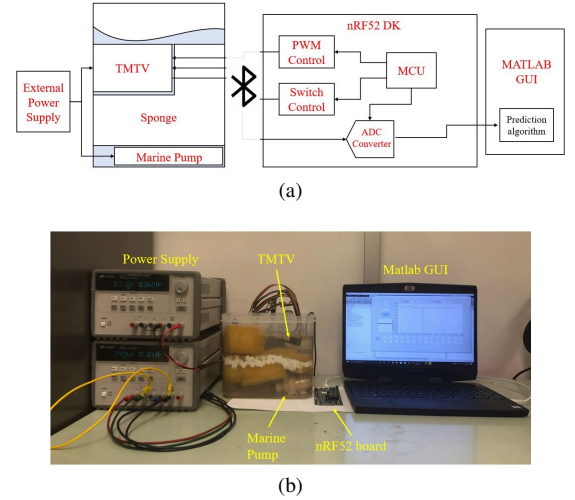

Fig. 9: (a) Illustration of hardware experiment system, (b) experiment set-up.

analog-to-digital converter (ADC) on the nRF52 board and are then transmitted to PC.

Two sets of experiments were conducted with this hardware testing system to evaluate the performance of the prediction algorithm under different types of PWM inputs. The range of PWM inputs admitted to the heat sources on TMTV is $[0, 10000]$ where 0 denotes a PWM signal with 100% duty cycle and 10000 denotes a PWM signal with 0% duty cycle. For each set of experiments, two different runs are conducted to investigate thermal effect of applying PWM inputs with same vs. different amplitudes to the two heat sources. The goal of applying inputs with different amplitudes is to investigate the effect of having modules of the IMD operating at different power levels. For the first set of experiments, randomly generated Gaussian PWM inputs are chosen to test the algorithm's prediction accuracy under randomness. In the first run, 2900 data samples generated using a Gaussian distribution within the range of $[1620, 10000]$ are used for both PWM inputs. For the case of Gaussian PWM inputs with different amplitudes, 3000 data samples are generated using two Gaussian distri-

butions within the range of $[5000, 10000]$ and $[7500, 10000]$ individually. For the second set of experiments, square wave inputs of length 2100 are used to evaluate the performance of the prediction algorithm when controller is implemented in real applications. Square wave inputs have a period of 20 seconds and the same duty cycle of 50%. The ranges of the square wave PWM inputs with different amplitudes are $[7500, 10000]$ and $[8750, 10000]$ respectively.

Similar to simulation studies, a batch data with randomly generated Gaussian inputs from a separate experiment is used for pre-processing for all experiments such that the recursive PBSID updating can be initiated after 10 seconds of the input and output data are obtained. As a result of the 10-fold crossvalidation with the batch data, regularization term λ is set as $\lambda = 0.3$. Thresholds values for surprise criterion T_1 and T_2 are calculated to be $T_1 = 15$ and $T_2 = 22$ via 10-fold crossvalidation. A fixed-lag Kalman smoother with a time lag of $N = 1$ is applied to the experiment data to reduce the noise in data. Process noise and measurement noise for the Kalman filter are assumed to be zero mean Gaussian random processes with variances $Q_k = 0.01^2$ and $R_k = 0.01^2$, respectively. For the prediction algorithm, normalized values of the PWM inputs are used and both non-spatial and spatial data components are detrended according to the batch data.

Figure 10 shows the experiment results when Gaussian inputs of different amplitudes are applied; more specifically, the overall prediction results of the algorithm (in red) are compared with the temperature data obtained by the heat sensors (in blue). For each comparison subplot in Figure 10, a zoomed plot is added to show the comparison of the prediction results and the temperature readings in more detail. Similar to results of the simulation studies, after approx. 400 sec. performance of the prediction results improve and the proposed algorithm can predict the instant changes in temperature readings with relatively high accuracy as can be see in Figure 10. In addition, Figure 11 shows the corresponding results for the square wave inputs with different amplitudes. As in Figure 10, a zoomed plot for each comparison subplot in Figure 11 is added to show the comparison of the prediction results and the temperature readings in more detail. There exists a small difference between the prediction results and the actual temperature data for some sensors, e.g. sensor 6 (S6) in Figure 10 and 11. This error in the prediction is larger for the experimental studies with square-wave inputs compared to the results of the experiments with Gaussian inputs. However, this prediction error is less than $0.4°C$ at any data point, which is below the critical temperature increase of $0.8°C$. Thus, the proposed prediction algorithm can still predict the thermal dynamics of the IMD with multiple heat sources. The accuracy of the prediction can be improved by further modifying the spatial weights matrix or alternatively by further modifying the kernel function used in the prediction of spatial data component.

In the experiments, the number of samples in the dictionary D_k is always under 20, i.e. $m < 20$, meaning that only approximately 1% of data points are used for prediction. The mean squared errors (MSEs) of the prediction results obtained via the proposed algorithm at given sensor locations, indicated
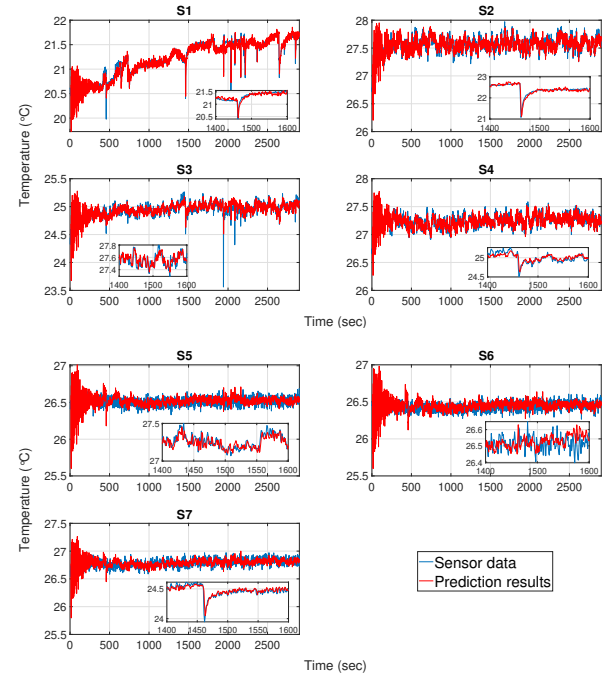

Fig. 10: Experiment results of the spatial and non-spatial data components combined for different Gaussian inputs; prediction results (*red*) and temperature readings (*blue*). Each subfigure shows the results at corresponding sensor locations labeled as S1-S6 in Fig. 8.
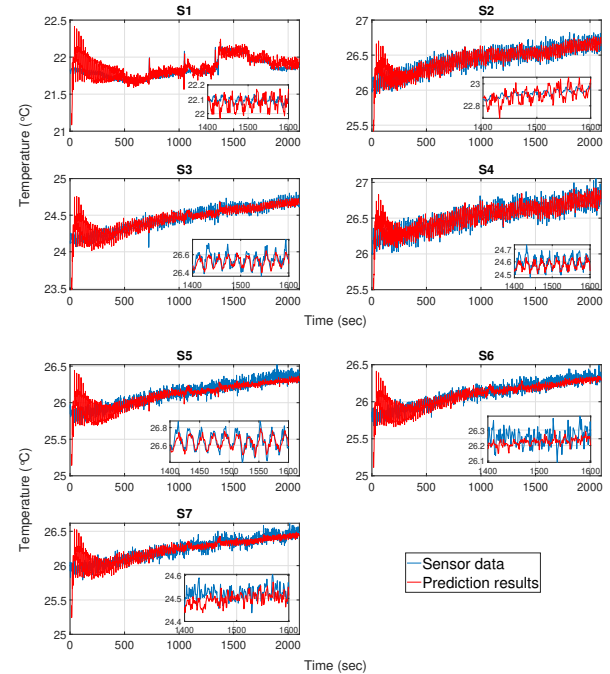

Fig. 11: Experiment results of the spatial and non-spatial data components combined for different square-wave inputs; prediction results (*red*) and temperature readings (*blue*). Each subfigure shows the results at corresponding sensor locations labeled as S1-S6 in Fig. 8.

TABLE III: OVERALL MSE RESULTS OF EXPERIMENTS ($^\circ C$)

S#	Gaussian Inputs		Square-Wave Inputs	
	Same Inputs	*Different Inputs*	*Same Inputs*	*Different Inputs*
S1	0.158	0.122	0.313	0.152
S2	0.160	0.124	0.315	0.151
S3	0.157	0.122	0.315	0.150
S4	0.159	0.122	0.316	0.15
S5	0.160	0.122	0.315	0.152
S6	0.158	0.122	0.333	0.151
S7	0.159	0.120	0.315	0.151

TABLE IV: NON-SPATIAL & SPATIAL PREDICTION RESULTS IN EXPERIMENTS ($^\circ C$)

MSE	Gaussian Inputs		Square-Wave Inputs	
	Same Inputs	*Different Inputs*	*Same Inputs*	*Different Inputs*
Non-spatial	0.156	0.119	0.313	0.149
Spatial	0.002	0.004	0.005	0.003

as S1, S2 etc., are summarized in Table III for each experiment study. In addition, Table IV summarizes breakdown of the MSE values of the prediction results corresponding to non-spatial vs. spatial identification parts of the algorithm. According to the results of the online prediction algorithm, which are compared with the temperature readings obtained by the on-board heat sensors, the spatially distributed thermal dynamics of an bio-implant with multiple heat sources can be predicted by the proposed algorithm with a mean squared error of $0.140 \, ^\circ C$ for Gaussian inputs and $0.243 \, ^\circ C$ for square-wave inputs. Due to convergence of the algorithm, the mean squared errors are reduced to $0.339 \times 10^{-2} \, ^\circ C$ and $1.405 \times 10^{-2} \, ^\circ C$ respectively after 400 seconds of operation. Compared with the results obtained in [14], our algorithm achieves prediction with relatively low MSE values while also characterizing the spatial autocorrelation among the sensor locations.

V. PERFORMANCE COMPARISON

In [11], researchers propose a batch-wise and a recursive PBSID method which use the high-order vector autoregressive with exogenous inputs (VARX) predictor from [12]. Similarly in [19], [20], PBSID methods proposed by Houtzager *et al.* in [11] and VARX model are used for identification of each local subsystem. In [14], Ermis *et al.* implemented both batch-wise and recursive PBSID methods with the PAST approach. In addition, multivariate linear regression (MLR) is a widely used method in statistics when there exist multiple independent and multiple dependent variables in the system. Using MLR method, the system behavior is modeled as $y_{i,k} = \alpha_i + \beta_{1,i} u_{1,k} + \beta_{2,i} u_{2,k}$ where $u_{j,k}, j = 1, 2$ are the power inputs at time instance k and α, β are the corresponding coefficients to be estimated. Another method used for the performance comparison is squared exponential Gaussian process regression (GPR). The squared exponential GPR method follows a similar regression model as the MLR method utilizing a kernel matrix in which the kernel function is of the form of a Gaussian distribution.

The proposed algorithm is compared with the aforementioned algorithms to evaluate its performance. A comparison of the MSE results of different identification schemes are shown in Figure 12. Since both in [19] and [11], PBSID methods with propagator method (PM) are used, we denote the algorithm as

PBSID_{pm} in the comparison figure. The algorithm used in [14] is denoted as PBSID_{past}. The multivariate linear regression method is denoted as MLR and the Gaussian process regression method is denoted as GPR. The COMSOL study with two different randomly generated Gaussian inputs is selected for the comparison.

According to the results presented in Figure 12, the proposed modeling algorithm performs overall significantly better compared to other algorithms in the literature. The performance of the proposed algorithm is similar to the performance of the GPR algorithm for all sensors except for sensor 3, i.e. S3. The main reason why the performances of both algorithms is similar for most sensor locations is that both algorithms utilize a kernel function of the form of a Gaussian distribution to model the heat dissipation at various sensor locations. The main difference between the two algorithms being that the proposed algorithm estimates the non-spatial component of the temperature increase first and then use the kernel function to determine the spatially dependent component of the heat dissipation. Thus, the proposed algorithm provides more accurate results at various sensor locations, especially for sensor 3.
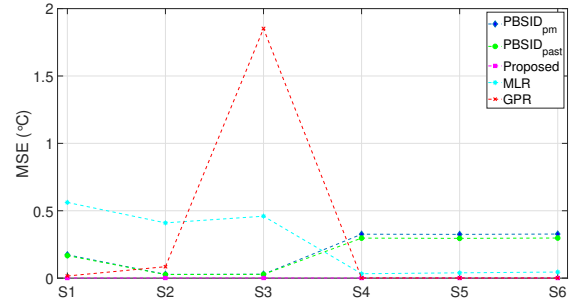

Fig. 12: Performance comparison of different identification schemes for COMSOL study 1 with different power inputs.

VI. CONCLUSION

Due to the technological advances in the medical field, capabilities of the implantable medical devices have significantly increased. Thus, modeling the thermal effect of implantable medical devices has gained importance to ensure thermal management of these devices for safe operation. In this paper, an online prediction algorithm is proposed to characterize the spatially correlated thermal effect of the IMDs with multiple heat sources and update the model parameters iteratively. Different from the previous work, our paper examines the online thermal prediction of IMDs with multiple heat sources using the spatially distributed on-board temperature sensors and aims to successfully characterize the spatial distribution of heat dissipation. Using a spatial filter, the algorithm filters out the spatially dependent component of the data. Then, the optimized PBSID methods are applied to the filtered data to predict the non-spatial data component and a KRLS filter with SC test is applied on a purely lagged SAR model for the spatially correlated data components.

To validate the proposed online prediction algorithm, numerous simulation studies are conducted with a COMSOL

model of the IMD. In addition, an *in vitro* experiment system with a custom developed TMTV is built. Results of both COMSOL simulation studies and *in vitro* experiments suggest that the proposed algorithm predicts the thermal effect of the implantable device with high accuracy. The prediction error decreases substantially after the convergence of the adaptive filters in the proposed algorithm. The results demonstrate that the proposed algorithm utilizing spatial filtering, subspace identification, and kernel adaptive filtering methods can successfully characterize the thermal effect of the IMD with multiple heat sources and spatially distributed temperature sensors. This indicates that the developed online thermal prediction algorithm can be used to model the thermal dynamics of an implantable medical device with multiple heat sources and support real-time optimal thermal and power management of IMDs.

REFERENCES

[1] M. Seemann, N. Zech, M. Lange, J. Hansen, and E. Hansen. "Anesthesiological aspects of deep brain stimulation : special features of implementation and dealing with brain pacemaker carriers," *Der Anaesthesist*, vol. 62, issue 7, pp.549-556, 2013. [Article in German]

[2] H. Duffau. "Contribution of cortical and subcortical electrostimulation in brain glioma surgery: Methodological and functional considerationsInterest of cortical and subcortical electrical stimuli in cerebral glioma surgery: methodological and functional considerations," *Clinical Neurophysiology*, vol. 37, issue 6, pp.373-382, 2007.

[3] N. L. Opie, A. N. Burkitt, H. Meffin, and D. B. Grayden, "Heating of the eye by a retinal prosthesis: modeling, cadaver and in vivo study," *IEEE Trans. on Biomed. Eng.*, vol. 59, pp. 339-345, 2012.

[4] K. Bazaka, M. V. Jacob, "Implantable Devices: Issues and Challenges," *Electronics*, vol. 2, pp.1-34, 2013.

[5] "Active Implantable Devices - Part 1: General requirements for safety, marking and information to be provided by the manufacturer," BS EN 45502-1:2015, European Standard, 2015.

[6] P. S. Ruggera, D. M. Witters, G. von Maltzahn, and H. I. Bassen, "In vitro assessment of tissue heating near metallic medical implants by exposure to pulsed radio frequency diathermy," *Physics in Medicine and Biology*, vol.48, pp.2919-2928, 2003.

[7] G. Lazzi, "Thermal effects of bioimplants," *IEEE Engineering in Medicine and Biology Magazine*, vol.24, no.5, pp.75-81, 2005.

[8] S. Kim, P. Tathireddy, R. A. Normann, and F. Solzbacher, "Thermal impact of an active 3-D microelectrode array implanted in the brain," *IEEE Transactions on Neural Systems and Rehabilitation Engineering*, vol.15, no.4, pp.493-501, 2007.

[9] S. C. DeMarco, G. Lazzi, W. Liu, J. D. Weiland, and M. S. Humayun, "Computed SAR and thermal elevation in a 0.25-mm 2-D model of the human eye and head in response to an implanted retinal stimulator-Part I: Models and methods," *IEEE Transactions on Antennas and Propagation*, vol.51, no.9, pp.2274-2285, 2003.

[10] R. Chai, Y. Zhang, "Adaptive Thermal Management of Implantable Device," *IEEE Sensors Journal*, vol. 19, issue 3, pp.1176 - 1185 2018.

[11] I. Houtzager, J. van Wingerden, and M. Verhaegen, "Recursive Predictor-Based Subspace Identification With Application to the Real-Time Closed-Loop Tracking of Flutter," *IEEE Transactions on Control Systems Technology*, vol. 20, issue 4, pp.934 - 949, 2012.

[12] A. Chiuso, "The role of vector auto-regressive modeling in predictor based subspace identification", *Automatica*, vol. 43, issue 6, pp.1034-1048, 2007.

[13] L. Ljung, "System Identification," in *The Control Systems Handbook: Control System Advanced Methods*, 2nd Edition, W. S. Levine, CRC Press, 2010, pp. 1275-1314.

[14] A. Ermis, Y. Lai, X. Pan, R. Chai, and Y. Zhang, "Recursive Subspace Identification for Online Thermal Management of Implantable Devices," *Proc. of 57th Allerton Conference on Communication, Control, and Computing*, 2019.

[15] S. Cho, J. Park, S. Sim *Sensors (Basel)*, vol. 15, issue 4, pp. 8131-8145, 2015.

[16] M. J. de Smith, M. F. Goodchild, P. A. Longley, *Geospatial Analysis*, 6th Edition, The Winchelsea Press, 2018.

[17] B.-C. Wang, H.-X. Li, and H.-D. Yang, "Spatial Correlation-Based Incremental Learning for Spatiotemporal Modeling of Battery Thermal Process," *IEEE Trans on Indus Electronics*, vol. 67, no. 4, 2020.

[18] Y. Feng, H. Li, "Dynamic Spatial-Independent-Component-Analysis-Based Abnormality Localization for Distributed Parameter Systems," *IEEE Transactions on Industrial Informatics*, vol. 16, issue 5, pp. 2929-2936, May 2020.

[19] A. Haber, P. R. Fraanje, M. Verhaegen, "Subspace Identification of Spatially Distributed Systems," *18th IFAC World Congress*, 2011.

[20] A. Haber, M. Verhaegen, "Identification of spatially distributed discrete-time state-space models," *16th IFAC Symposium on System Identification*, 2012.

[21] C. T. Wentz, J. G. Bernstein, P. Monahan, A. Guerra, A. Rodriguez, and E. S. Boyden, "A wirelessly powered and controlled device for optical neural control of freely-behaving animals," *Journal of Neural Engineering*, vol.8, no.4, 2011.

[22] A. Getis, D. A. Griffith, "Comparative Spatial Filtering in Regression Analysis," *Geographical Analysis*, vol. 34, pp. 130-140, 2002.

[23] D. Griffith, Y. Chun, "Spatial Autocorrelation and Spatial Filtering," *Handbook of Regional Science*, Germany: Springer, chapter 75, pp. 1477-1507,2014.

[24] J. Thayn, "Eigenvector Spatial Filtering and Spatial Autoregression", *Encyclopedia of GIS*, Springer, 2017.

[25] A. Chiuso, G. Picci, "Consistency analysis of some closed-loop subspace identification methods," *Automatica*, vol. 41, no. 3, pp.377-391, 2005.

[26] B. Yang, "Projection approximation subspace tracking," IEEE Transactions on Signal Processing, vol. 43, no. 1, pp. 95-107, 1995.

[27] Y. Engel, S. Mannor, R. Meir, "The Kernel Recursive Least-Squares Algorithm," *IEEE Transactions on Signal Processing*, vol. 52, no. 8, 2004.

[28] J. Kabbara, "Kernel Adaptive Filtering Algorithms with Improved Tracking Ability," M.S. Thesis, Department of Electrical and Computer Engineering, McGill Univ., Montreal, Canada, April, 2014. Accessed on: Aug. 28, 2019. [Online].

[29] W. Liu, J. C. Principe, and S. Haykin, *Kernel Adaptive Filtering: A Comprehensive Introduction*, John Wiley & Sons, Inc., 2010.

[30] S. Fantini, A. Sassaroli, K. T. Tgavalekos, and J. Kornbluth,"Cerebral blood flow and autoregulation: current measurement techniques and prospects for noninvasive optical methods," *Neurophotonics*, vol. 3, issue 3, Jul. 2016.